pH-sensing hybrid hydrogels for non-invasive metabolism monitoring in tumor spheroids

Riccardo Rizzo [a,1], Valentina Onesto [a,1], Giulia Morello [a,b,1], Helena Iuele [a], Francesca Scalera [a], Stefania Forciniti [a], Giuseppe Gigli [a,b], Alessandro Polini [a,**], Francesca Gervaso [a,2], Loretta L. del Mercato [a,*,2]

[a] *Institute of Nanotechnology, National Research Council (CNR-NANOTEC), C/o Campus Ecotekne, Via Monteroni, 73100, Lecce, Italy*
[b] *Department of Mathematics and Physics "Ennio De Giorgi", University of Salento, C/o Campus Ecotekne, Via Monteroni, 73100, Lecce, Italy*

ARTICLE INFO

ABSTRACT

The constant increase in cancer incidence and mortality pushes biomedical research towards the development of *in vitro* 3D systems able to faithfully reproduce and effectively probe the tumor microenvironment. Cancer cells interact with this complex and dynamic architecture, leading to peculiar tumor-associated phenomena, such as acidic pH conditions, rigid extracellular matrix, altered vasculature, hypoxic condition. Acidification of extracellular pH, in particular, is a well-known feature of solid tumors, correlated to cancer initiation, progression, and resistance to therapies. Monitoring local pH variations, non-invasively, during cancer growth and in response to drug treatment becomes extremely important for understanding cancer mechanisms. Here, we describe a simple and reliable pH-sensing hybrid system, based on a thermoresponsive hydrogel embedding optical pH sensors, that we specifically apply for non-invasive and accurate metabolism monitoring in colorectal cancer (CRC) spheroids. First, the physico-chemical properties of the hybrid sensing platform, in terms of stability, rheological and mechanical properties, morphology and pH sensitivity, were fully characterized. Then, the proton gradient distribution in the spheroids proximity, in the presence or absence of drug treatment, was quantified over time by time lapse confocal light scanning microscopy and automated segmentation pipeline, highlighting the effects of the drug treatment in the extracellular pH. In particular, in the treated CRC spheroids the acidification of the microenvironment resulted faster and more pronounced over time. Moreover, a pH gradient distribution was detected in the untreated spheroids, with more acidic values in proximity of the spheroids, resembling the cell metabolic features observed *in vivo* in the tumor microenvironment. These findings promise to shed light on mechanisms of regulation of proton exchanges by cellular metabolism being essential for the study of solid tumors in 3D *in vitro* models and the development of personalized medicine approaches.

1. Introduction

Neoplasia represents the leading cause of death on a global scale and the value of cancer incidence and mortality is growing rapidly worldwide. Among all cancer types, about one-third of mortality and incidence is related to gastrointestinal cancer [1]. Although the development of different treatment strategies has been successful in extending up to two years the survival of patients with metastatic gastrointestinal cancer, there is still no efficient therapy on long-term patient survival [2,3]. New

therapeutic approaches are urgently needed for gastrointestinal cancer at advanced stages but, in order to discover rapidly effective treatments, good models that faithfully reproduce the cancer disease mechanisms in humans are mandatory and, unfortunately, not available yet [4]. In this regard, many experimental systems fail in reproducing the heterogeneity of tumors [5,6]: for instance, in adherent 2D cell culture models cells grow as a monolayer, without mimicking the natural structures of tissues or tumors. Consequently, they do not adequately represent cell-cell and cell-extracellular environment interactions [7] and often fail in

---

identifying drugs that can be successfully translated to clinical oncology [8]. On the other hand, animal models can simulate a higher degree of complexity, but costs, ethical considerations, and species heterogeneity frequently preclude the application of treatments to humans [9]. These disadvantages led to the development of three-dimensional (3D) culture systems, such as organoids and spheroids, that better replicate *in vivo* conditions [7,10,11]. Typically, animal extracellular matrix materials (*i.e.*, Matrigel) are used in organoid cultures [12], but they can cause lack of reproducibility of cell culture experiments due to their variable composition and properties within the single batch and between different batches; additionally, they have antigenicity potential being they animal-derived [13].

Natural and synthetic hydrogels have therefore been proposed for the development of *in vitro* tumor models, to reproduce the 3D tumor architecture physically and chemically [14]. Hybrid hydrogels, characterized by the synergistic interaction of two or more biopolymers, provide the opportunity of covering a wider range of physicochemical features [15,16]. Among this class of materials, a natural polymer-based hydrogel, composed of chitosan and pectin, has been successfully used for cell embedding and culturing [17–19]. Chitosan is a linear natural cationic polysaccharide derived from chitin that is found in crustaceans' exoskeletons and fungi, and pectin a linear, highly available, biodegradable and non-toxic, anionic plant heteropolysaccharide [20]. The combination of these two polysaccharides leads to the formation of a stable semi-interpenetrating network (semi-IPN). More in detail, the chitosan capacity to create a polymeric hydrogel network by increasing temperature, in the presence of a gelling agent, *e.g.*, beta-glycerophosphate (βGP), has been exploited to incorporate a second polymer, *i.e.*, pectin. The resulting system comprises a chitosan/βGP physically "cross-linked" network and one branched polymer, pectin, that are not covalently bonded to each other, but partially interlaced on a molecular scale, originating a semi-IPN [21]. Chitosan-pectin (Ch/Pec) hydrogel is thermoresponsive at 37 °C and can be processed at mild conditions to embed cells or tumor spheroids [17,18], with the aim of mimicking the original tumor microenvironment (TME).

The TME is characterized by unique features, such as acidic pH conditions, rigid extracellular matrix, altered vasculature, hypoxic condition [22], that all contribute to feed the tumor and represent a barrier to drugs. In particular, acidification of extracellular pH is a well-known hallmark of solid tumors that leads to cancer initiation, progression, and resistance to therapies [23–26]. The accumulation of protons (H$^+$) in the extracellular microenvironment is the result of a deficient blood perfusion, with consequent hypoxia and accumulation of acidic metabolic waste products [27]. In addition, cancer cells present high metabolic demand and they shift towards glycolytic metabolism, decreasing mitochondrial oxidative phosphorylation, through the so-called Warburg effect [25]. This metabolic reprogramming protects cancer cells from oxidative stress, increases their resilience to hypoxia, and causes enormous glucose absorption [28]. Consequently, monitoring local pH is essential for understanding the biology under tumor development and as metabolic readout for cancer detection and therapy [29–33].

Mapping extracellular pH in tumor is extremely challenging, because of the complexity of the microenvironment, which is a network of cellular and extracellular matrix components [34,35]. At present, several tools are available to measure extracellular acidification in living cells, such as conventional extracellular flux analyzers (*i.e.*, Seahorse analyzers) [36] and label-free pH nanoprobes [37]. Each of these methods offer different advantages for pH sensing. However, they inherently suffer of limited spatio-temporal resolution, are more invasive than optical methods [38] and can mainly be used to measure average values of extracellular acidification. Conversely, individual cell extracellular pH can be imaged by surface-enhanced Raman spectroscopy (SERS), which has ultrahigh sensitivity and good spatial resolution, but needs to be combined with plasmonic nanostructures of well-defined and uniform geometry and pH-sensing Raman reporters with highly selective and non-toxic properties [39–43].

Among the optical approaches, pH sensors based on ratiometric fluorescence changes have emerged for single-cell and real-time analyses due to their minimally invasive nature and high measurement reliability that is unaffected by changes in sensor concentration, instrument sensitivity, and environmental factors [44–51]. Compared to single emission intensity, ratiometric sensors provide measurements of the fluorescence intensity ratio at two different emission wavelengths, which is then correlated with pH levels. For example, here, pH is obtained ratiometrically by using fluorescein isothiocyanate (FITC) as pH-sensing dye and rhodamine B isothiocyanate (RBITC) as reference dye. Indeed, FITC is sensitive to pH changes thanks to the presence of ionizable groups that cause a decrease in fluorescence emission as H$^+$ concentration increases [52].

In this scenario, it emerges clearly that it is crucial to generate robust and biocompatible *in vitro* systems that, on one hand, closely resemble geometry and structure of solid tumors [11,53] and, on the other, are able to capture a peculiar feature of TME, *i.e.*, the spatio-temporal pH gradients.

Therefore, here, with the aim of developing a non-invasive platform for the spatio-temporal detection of pH in the extracellular microenvironment of colorectal cancer (CRC) spheroids, we *(i)* integrated, within our previously developed Ch/Pec hydrogel systems, recently devised optical ratiometric pH sensors and *(ii)* used this hybrid platform to validate the response to drugs for personalized oncological treatments.

2. Results and discussion

2.1. Fabrication of pH-sensing hybrid Ch/Pec hydrogels

We fabricated a pH-sensing hybrid platform for the spatio-temporal extracellular pH mapping in 3D cell culture by embedding recently devised fluorescent ratiometric pH sensors, based on silica (SiO$_2$) microparticles functionalized with fluorescein isothiocyanate (FITC), as pH indicator probe, and rhodamine B isothiocyanate (RBITC), as reference dye [54], within our optimized Ch/Pec hydrogel system [17,18]. The fabrication procedure is shown in Fig. 1. The first step involves the sequential addition of CRC spheroids and pH sensors into the Ch/Pec formulation (Fig. 1a and b). We selected the Ch/Pec system because it is a thermoresponsive hydrogel composed by a natural polymer, chitosan, able to cross-link with a weak base, leading to the formation of a stable network that entraps a second natural polymer, pectin, generating a semi IPN system. The system is injectable at room temperature (RT) and presents the sol-gel transition at physiological temperature [17], a key feature for being applied also *in vivo* as *in situ* sensing platform that spontaneously solidify into a hydrogel near the body temperature and noninvasively report local changes of pH over time and space. Notably, its porous structure and suitable permeability allow the transport of nutrients, oxygen, and metabolites, supporting the growth and culture of CRC cancer cell line also in a long-term period [18]. HCT116 spheroids and 40 μL of pH sensors (5.38×10^6 particles/mL stock solution) per each mL of Ch/Pec, are dispersed in complete DMEM medium and mixed with Ch/Pec hydrogel in 3:1.5 ratio. The second step, the gelation step at 37 °C (20 min), yields to pH-sensing hybrid Ch/Pec hydrogels (Fig. 1c). In the third step, 50 μL of the hydrogel mixture are deposited in individual wells of an 8-well chamber slide for calibration and timelapse imaging purposes (Fig. 1d): the calibration curve, that correlates fluorescence intensity ratio of FITC and RBITC channels (I$_{FITC}$/I$_{RBITC}$) with pH values, is obtained by exposing spheroids to pH-adjusted cell medium. In the fourth step, hydrogels are imaged via 4D (x,y,z,t) confocal laser scanning microscopy (CLSM) for 6 h (time points: 30 min) (Fig. 1e). The fifth step involves segmentation of CLSM records through a custom algorithm to obtain centroids and I$_{FITC}$/I$_{RBITC}$ ratios of each sensor particle and then, by passing I$_{FITC}$/I$_{RBITC}$ values to the calibration curve, a spatio-temporal pH map around individual spheroid (Fig. 1f).
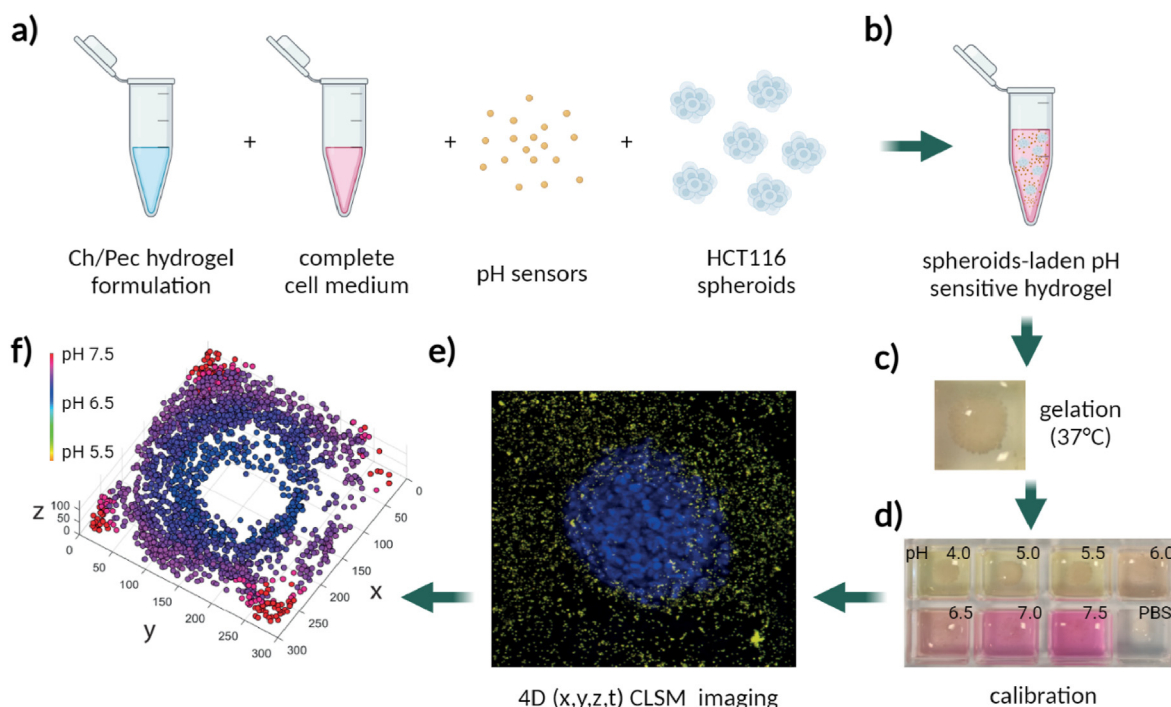
Fig. 1. **Schematics (not drawn to scale) of the fabrication process of hybrid** pH **sensing Ch/Pec hydrogels for spatio-temporal sensing of extracellular acidification of CRC spheroids. (a–b)** Sequential addition of HCT116 spheroids and pH sensors, dispersed in complete DMEM medium (3:1.5 ratio), into chitosan-pectin formulation. **(c)** Gelation step at 37 °C (20 min). **(d)** Calibration of the hybrid pH sensing Ch/Pec hydrogels in pH-adjusted cell medium. **(e)** CLSM (x,y,z,t) timelapse imaging of hybrid pH sensing Ch/Pec hydrogels (6 h, time points: 30 min). **(f)** Image segmentation and data analysis for obtaining a spatio-temporal pH map around each spheroid.

2.2. Characterization of hybrid pH-sensing Ch/Pec hydrogels

The properties of Ch/Pec hydrogels embedding pH sensors (Ch/Pec +) were compared to those of Ch/Pec hydrogels without pH sensors (Ch/Pec –). As regards the hydrogel's suitability for cell-encapsulation, the pH values of the starting polymer and βGP solutions as well as of the final hydrogel were measured. Despite the acidic pH values of the starting solutions (equal to 6.0 and 5.0 for Ch and Pec solutions, respectively), the Ch/Pec system reached a neutral pH value (pH = 7.4) immediately after

mixing with DMEM, used to simulate cell encapsulation and to disperse the pH sensors into the system. Notably, the addition of the optical sensors did not alter the pH. .

The Ch/Pec + and Ch/Pec – hydrogel, as prepared, resulted both injectable at RT through a G23 needle (Videos S1, S2). The inversion tube test indicated that the presence of pH sensors did not alter the thermoresponsive behavior of Ch/Pec hydrogel showing that, as injected at RT, both hydrogel solutions flow along the vial walls when the vial was turned; conversely, after 2 h of incubation at 37 °C, the hydrogels could
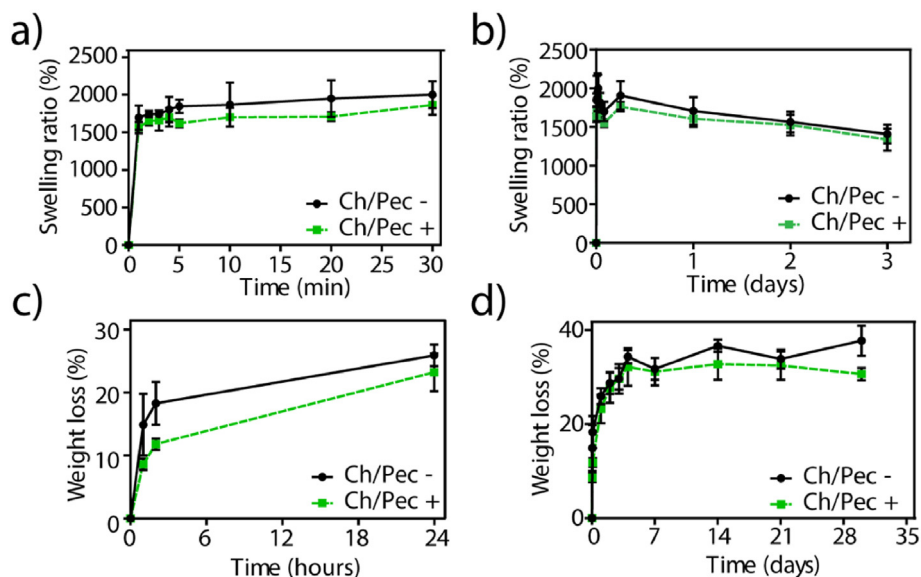

Fig. 2. **Stability of hybrid pH sensing Ch/Pec hydrogels. (a–b)** Swelling test results of Ch/Pec + and Ch/Pec – after 30 min (a) and after 3 days (b) of incubation at 37 °C. **(c–d)** Weight loss percentage of Ch/Pec + and Ch/Pec – after 24 h (c) and after 30 days (d) of incubation at 37 °C.

not flow anymore and the sol-gel transition process was completed for both the formulations (Fig. S1, Videos S3, S4).

Supplementary video related to this article can be found at https://doi.org/10.1016/j.mtbio.2023.100655.

The swelling and *in vitro* stability tests, performed on Ch/Pec + and Ch/Pec − hydrogels, showed that both formulations had a high swelling ability already in the first 5 min of incubation in PBS at 37 °C (Fig. 2a).

Although the two hydrogels show a comparable trend, the Ch/Pec − hydrogels displayed a higher swelling ratio (~2000%) in the first 30 min of incubation as compared to the Ch/Pec + hydrogels (~1600%), reducing their differences over time (Fig. 2b). Notably, both formulations reached equilibrium very quickly after a few hours (Fig. S2a), while, after one day of incubation, a slow degradation process likely started, though the swelling properties of all the samples remained stable up to two weeks (Fig. S2b). Stability testing allowed to evaluate the degradation kinetics up to 30 days of incubation at 37 °C. The weight loss % showed a comparable trend for the two formulations, presenting a higher increase in the first 12 h, reaching its maximum on the third day of incubation, and remaining almost constant up to day 21 (Fig. 2c). Though no statistical differences were recorded among the two hydrogels, Ch/Pec + showed lower values of weight loss % in the first day of incubation (Fig. 2d).

Next, the rheological properties of the hydrogels were studied by strain sweep, frequency sweep, time sweep and temperature sweep tests. The first test aimed to check for the linear viscoelastic (LVE) limit by performing a strain sweep on a fully formed gel. The results of the strain sweep are shown in Fig. 3a and b. The storage modulus G′ was higher than the loss modulus G″ at each strain value, as expected for fully
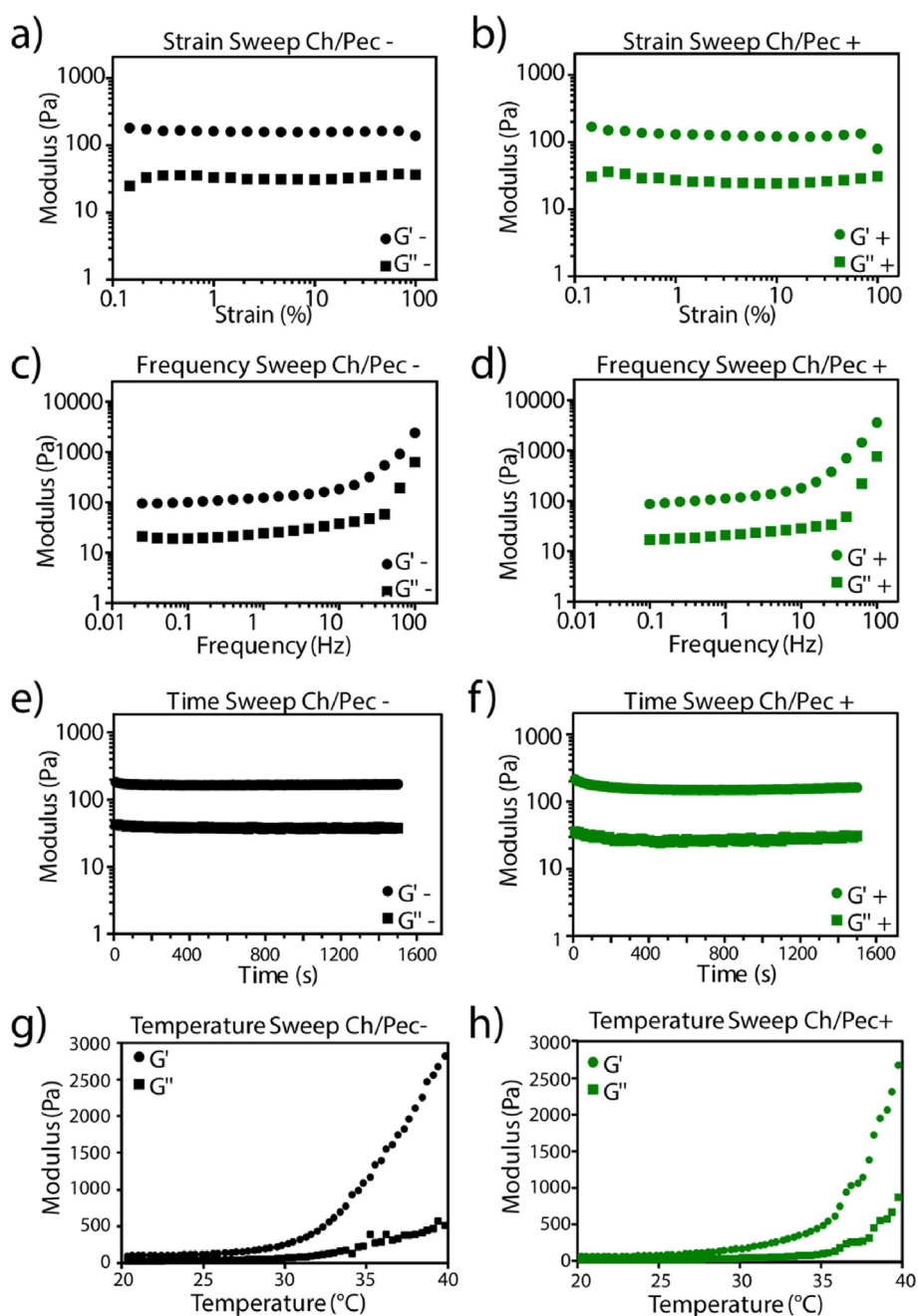

Fig. 3. Rheological properties of hybrid pH sensing Ch/Pec hydrogels. Hydrogel storage modulus (G′) and loss modulus (G″), for each formulation from strain sweep (**a–b**), frequency sweep (**c–d**), time sweep (**e–f**) and temperature sweep tests (**g–h**).

formed hydrogels. Both formulations showed linear behavior (constant values as strain is varied) from 0.3 to 50% strain and therefore a strain of 10% was selected for subsequent sweeps. The frequency sweep test (Fig. 3c and d) showed a linear behavior for frequency values lower than 10 Hz, hence, a value equal to 1 Hz was selected for the subsequent time sweep test.

Time sweep tests (Fig. 3e and f) indicated that both formulations led to fully formed and stable hydrogels (G'>G'' and both moduli constant in the analyzed time range). Importantly, the obtained data show that, overall, the presence of pH sensors inside Ch/Pec hydrogels did not affect the shear mechanical properties of the hybrid system. Finally, the temperature sweep tests (Fig. 3g and h) show a significant increase in G' value when the temperature reaches the physiological value, confirming that the proposed hydrogel formulations are thermoresponsive. Moreover, the results of the temperature sweeps test allowed to verify that the pH sensors did not alter the thermal responsiveness of the Ch/Pec hydrogel. The mechanical properties of hybrid hydrogels were measured by compression tests (Fig. 4). The stress-strain curves showed a similar non-linear behavior between the two hydrogels, presenting an increase in

the stress values as the compressive strain increased. However, as shown in Fig. 4a and b, the introduction of pH sensors into the Ch/Pec hydrogel system induced a significant increase in its mechanical properties in compression with a significantly higher Young's modulus. Overall, the compression test showed that both formulations have a very low Young's modulus (between 3 and 5 kPa).

The morphology of the hybrid pH-sensing Ch/Pec hydrogels was analyzed by scanning electron microscope (SEM) image acquisitions. The critical point drying (CPD) technique was used to dehydrate the hydrogels preserving their original pore structure, which would otherwise be affected by conventional freeze-drying processing. Representative SEM images from CPD-dried hydrogels are shown in Fig. 5a–d at different magnifications. The Ch/Pec formulations were characterized by a highly interconnected porous structure, with a branched and random architecture. The addition of the pH sensors did not affect the morphological characteristics of the system, but, on the contrary, they seemed to establish interactions with the gel network, being wrapped by the fibers network of the hydrogel. An estimation of the apparent pore diameter was performed through image analysis: the average values were $0.34 \pm$
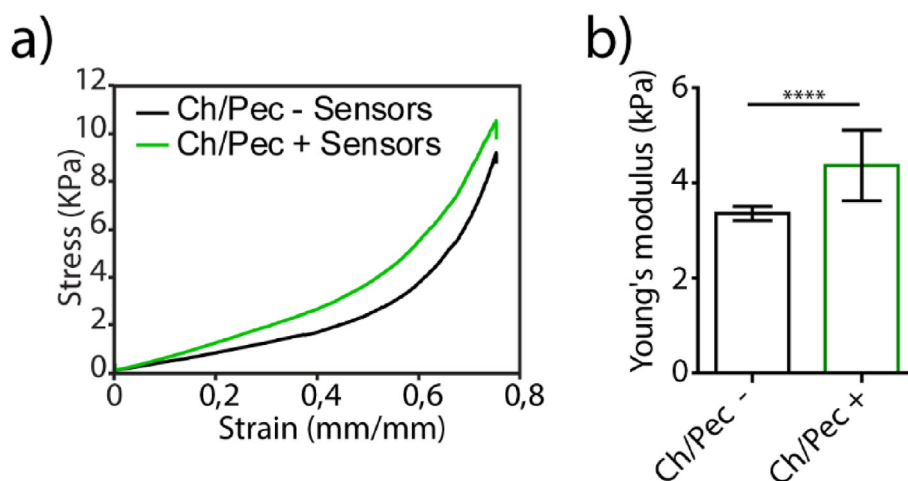

Fig. 4. Mechanical properties of hybrid pH sensing Ch/Pec hydrogels. Compression test results of the two hydrogel formulations, Ch/Pec + and Ch/Pec −. Stress strain curves **(a)** and Young's modulus **(b)**. The values are reported as mean ± standard deviation (n = 4). *$\leq$0.05, ****$\leq$0.0001 (Two-way ANOVA test).
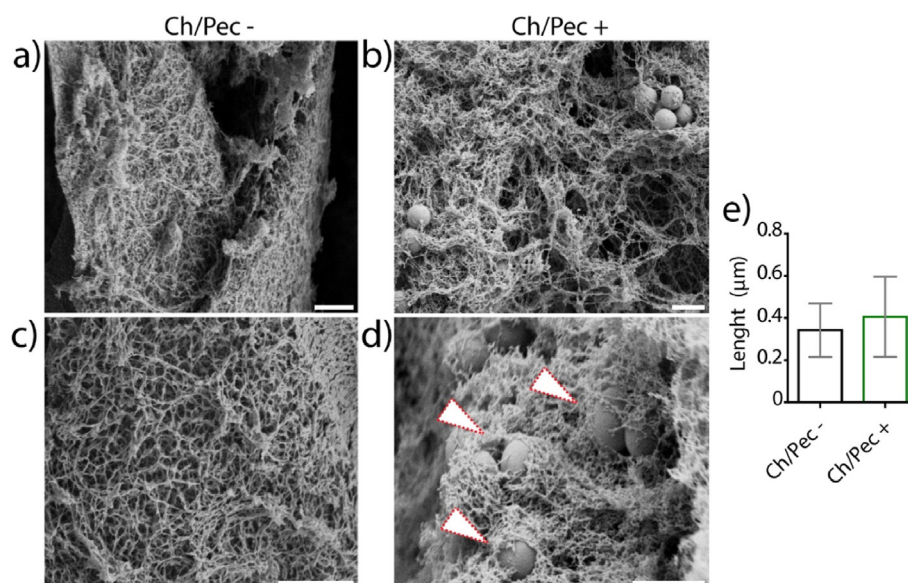

Fig. 5. Morphology of Ch/Pec − and Ch/Pec + hydrogels. (a–d) Representative SEM images of (a,c) Ch/Pec − and **(b,d)**Ch/Pec + hydrogels (SEM mode, 10k × (a,b) and 20k × (c,d) magnifications). Arrowheads indicate pH sensors. The integration of the pH sensors in the hydrogel fiber network can be appreciated. **(e)** Average values and standard deviations of the pore size of hydrogel formulations with and without the addition of pH sensors. Scale bars, 2 μm.

0.12 μm and 0.40 ± 0.19 μm for Ch-Pec – and Ch-Pec +, respectively, with comparable values between the two formulations (Fig. 5e).

Geometry and complexity of a scaffold can deeply affect solute diffusivity [55] and the three-dimensional crosslinked fibrous network of the hydrogel, thanks to its high porosity, multi-scale pore size distribution and interconnectivity of the pores promotes the transport of biologically active compounds (e.g., drugs), nutrients and signaling molecules [56,57]. As a consequence, gradients of small ions such as H^+, spatially distributed around the cells, can be effectively registered by the pH sensors trapped within the Ch/Pec network.

Finally, the *in vitro* biocompatibility of Ch/Pec – and Ch/Pec + hydrogels was assessed by the calcein AM/propidium iodide live/dead assay. Data reported in Fig. 6a–c shows that HCT116 spheroids remained viable until day 7 in all tested conditions, with the occurrence of only few red spots indicative of dead cells. In parallel, the culture medium of Ch/Pec – and Ch/Pec + hydrogels were used to quantitatively determine cell viability by the Presto blue™ assay (Invitrogen, Thermo Fisher Scientific). As shown in Fig. 6d, HCT116 spheroids in Ch/Pec – and Ch/Pec + hydrogels exhibited high cell viability over time confirming the biocompatibility of Ch/Pec hydrogels.

2.3. pH-sensitivity of Ch/Pec + hydrogel

To test the response of pH sensors within the hydrogel, SiO_2-based pH sensors were integrated in the hydrogel (see experimental section) and then exposed to different pH-adjusted cell media for 30 min before being imaged by CLSM. Different images were collected along the z-axis of the 3D Ch/Pec + hydrogels. Fig. 7a shows representative images of Ch/Pec
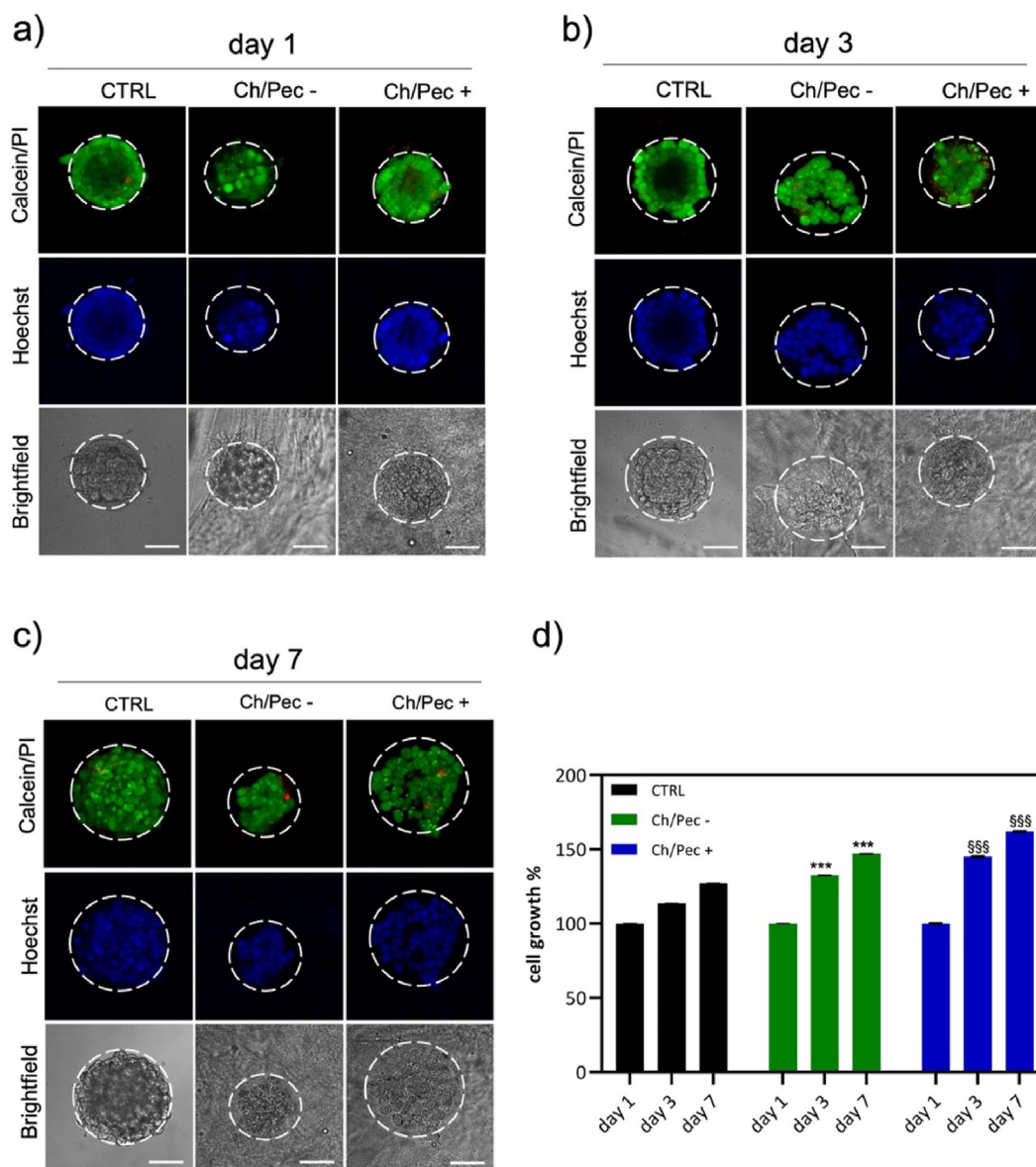

Fig. 6. *In vitro* **biocompatibility of Ch-Pec hydrogels. (a–c)** Live/dead-stained spheroids and Ch-Pec hydrogel formulations acquired at 1, 3 and 7 days. The HCT-116 spheroids were stained with calcein AM (green, live cells), PI (red, dead cells) and Hoechst (blue, nuclei). Spheroids without hydrogel formulations were used as control (CTRL). Dashed lines indicate the edge of the spheroids. Scale bars 50 μm. The Z-stacks were obtained using a LSM700 confocal microscope (Zeiss S. p.A.) at 20× magnification. The maximum intensity projection was generated from 11 z-stacks images for the CTRL and from 22 z-stacks images for Ch/Pec + or Ch/Pec – (z-stack step size = 2.55 μm). **(d)** Cell viability assay of HCT-116 spheroids encapsulated in Ch/Pec + and Ch/Pec – hydrogels measured by PrestoBlue® Reagent at 1, 3 and 7 days. Cell growth percentage over time was normalized on day 1 of each condition. Spheroids without hydrogel formulations were used as control (CTRL). Values represent the means (±SE) of three independent experiments. Statistical analysis: ***p < 0.001, CTRL *vs.* Ch/Pec -, §§§p < 0.001, CTRL *vs.* Ch/Pec +.
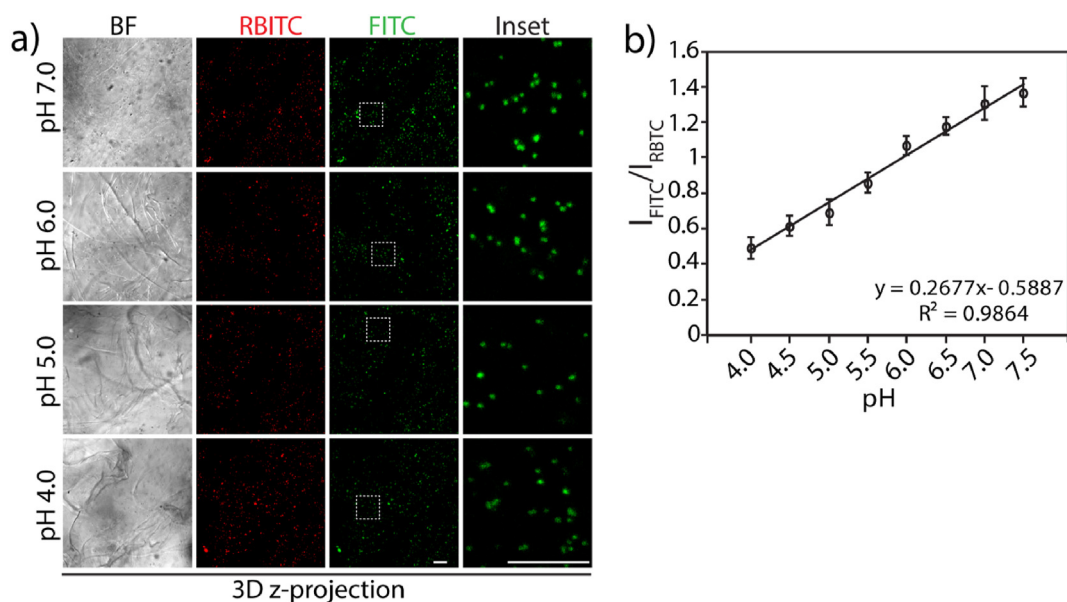
Fig. 7. Calibration of hybrid pH-sensing Ch/Pec hydrogels. (a) Representative CLSM images showing Ch/Pec hydrogels (maximum intensity z-projection) containing pH sensor microparticles exposed to different pH-adjusted cell media. FITC (green channel), RBITC (red channel), bright field (BF, grey channel) are shown. Dashed boxes indicate the inset regions. Z-projections of 6 sections for each indicated pH. Z-stack step size = 2.27 μm. Scale bars: 50 μm. **(b)** Ratiometric calibration curve of hybrid pH-sensing Ch/Pec hydrogels shown in (a). The fluorescence intensity ratio of green (I_{FITC}) and red (I_{RBITC}) channels was calculated for each pH sensor (see experimental section) and their mean for the tested pH values is reported in the graph. Data are means ± SEM.

+ hydrogels incubated at pH 4.0, 4.5, 5.0, 5.5, 6.0, 6.5, 7.0 and 7.5, respectively. According to the optical properties of the selected dyes, the pH indicator dye (FITC, green) showed increased fluorescence under increasing pH values [52,58], while the fluorescence intensity of the reference dye (RBITC, red) was not altered. CLSM images were then processed with a customized algorithm to automatically extract positions and intensity ratio (I_{FITC}/I_{RBITC}) of the sensors for each pH value [54]. Next, the values were plotted as function of pH, displaying a linear pH-dependent calibration curve (Fig. 7b) in the range between pH 4.0 and pH 7.5, with a high correlation coefficient R^2. Calibration was performed at the beginning of each experiment and used to measure, by resolving the equation of the fit calibration curve, the pH read out of sensors located in the Ch/Pec hydrogel under evaluation. The linear pH sensitivity of the pH sensors was in accordance with our previous work [54], where it was even demonstrated the good reversibility and stability over time of the microparticles, making them highly suitable for spatio-temporal acidification analyses in biological systems.

Structure, preparation of the Ch/Pec hydrogel and microparticle-polymer ratio were adjusted in order to obtain a homogeneous distribution of the sensors and to prevent their aggregation, resulting in a fibrous hydrogel network exhibiting high surface-to-volume ratio and porosity, which favors the transport of H^+ ions across the scaffold. This supports the use of Ch/Pec + hydrogels as 3D pH-sensing scaffold for detecting acidic-base metabolic variations generated by CRC spheroids culture under different experimental conditions.

2.4. Spatio-temporal mapping of extracellular pH in hybrid Ch/Pec + hydrogel with CRC spheroids

To map the proton gradients generated by CRC spheroids over time and space and to monitor their behavior under drug treatment, HCT116 spheroids were encapsulated in Ch/Pec + hydrogel as described before (see experimental section and scheme in Fig. 1). Samples were then treated with vehicle (control) or 5-Fluorouracil (5FU) (10 μM) for 24 h before proceeding with the 4D CLSM imaging (Fig. 8b-c). Importantly, the calibration of hybrid pH-sensing Ch/Pec + hydrogels was performed before imaging the control and treated spheroids, respectively.

After imaging the samples, the positions of the ratiometric pH sensors were automatically detected by a customized algorithm as described in the experimental section, and the pH response was evaluated at different distances from the spheroid's centroids as shown in the cartoon in Fig. 8a. The pH measured by each sensor was extrapolated from the pH calibration formula [54]. Then, 3D scatter plots with a colormap linked to pH data values were generated for control and treated HCT 116 spheroids embedded in the thermosensitive Ch/Pec + hydrogels, and the spatial distribution of the sensors and their pH dynamic changes over time were monitored, respectively.

Each sensor shows a specific color which strongly depends on **i.** The time point (t) at which the measurement was performed and **ii.** The position of the sensor, along the x, y, z axes, respect to the centroid of the spheroid under evaluation. Therefore, the heterogeneous distribution of protons generated by HCT 116 spheroids can be visualized in Ch/Pec hydrogel under both control and treated conditions (Fig. 9a and b and Videos S5, S6). The pH response of ratiometric pH sensors surrounding the spheroids was quantified and expressed as a mean as shown in Fig. 9c and d. Ratiometric fluorescence-based pH sensors were previously integrated in alginate hydrogel-based 3D co-cultures of tumor and stromal pancreatic cells, where localized and reversible pH sensing was achieved with micrometer-scale spatial resolution [54]. Here, the use of a Ch/Pec hydrogel allowed to extend this type of analysis to multicellular aggregates (spheroids) and analyze the proton gradient distribution in the spheroid proximity.

In particular, in control conditions the microenvironment surrounding the HCT116 spheroid showed a pH value of 7.1 which was registered a time 0 and remained constant till 90 min before slowly decreasing over time reaching a value of pH 6.3 after 360 min (Fig. 9c), similarly to pH values detected in tumor microenvironment *in vivo.* [25,59].

For 5FU treated spheroid the pH measured at time 0 was 7.1, similarly to control condition, however the decrease of pH observed over time was faster and more pronounced, thus reaching a value of pH 5.7 already after 90 min, which further dropped down over time reaching pH 4.9 at 360 min (Fig. 9d). Overall, the general trend observed in both control and treated conditions revealed an acidification of the microenvironment over time (Fig. 9a–d), which was marked in HCT116 treated spheroids (Fig. 9b, d).
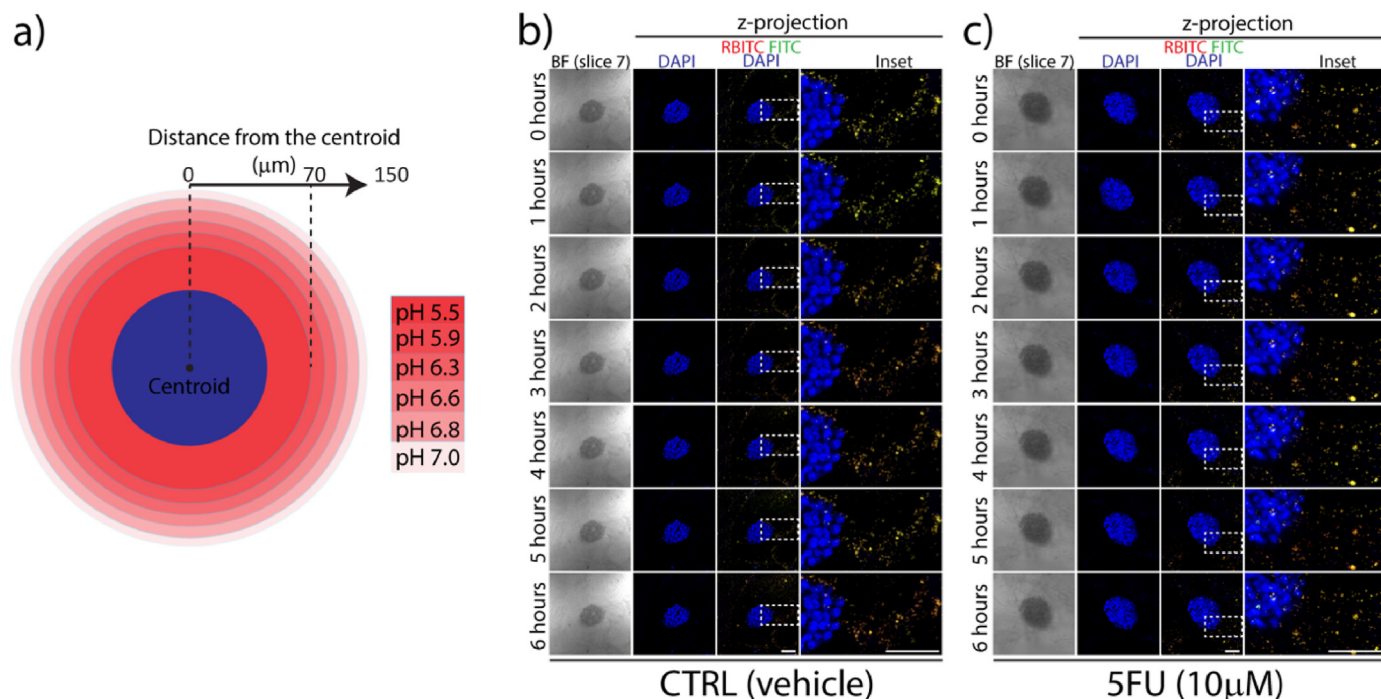
Fig. 8. HCT116 spheroids extracellular pH evaluation in time and space under 5FU treatment. **(a)** Schematic representation of a HCT116 spheroid (blue) embedded in Ch/Pec + hydrogel (z-projection). Red circles at different color gradient indicate hypothetical pH gradients generated at different distances from the centroid. **(b,c)** Representative images of 4D CLSM of HCT116 spheroids embedded in Ch/Pec + hydrogels (maximum intensity z-projection of 14 sections) containing pH-sensing particles (FITC, green; RBITC, red) and treated with vehicle (CTRL) or 5FU (10 μM) for the 24 h. BF, grey; DAPI, blue. Dash boxes indicate the crop region. Scale bars, 100 μm.
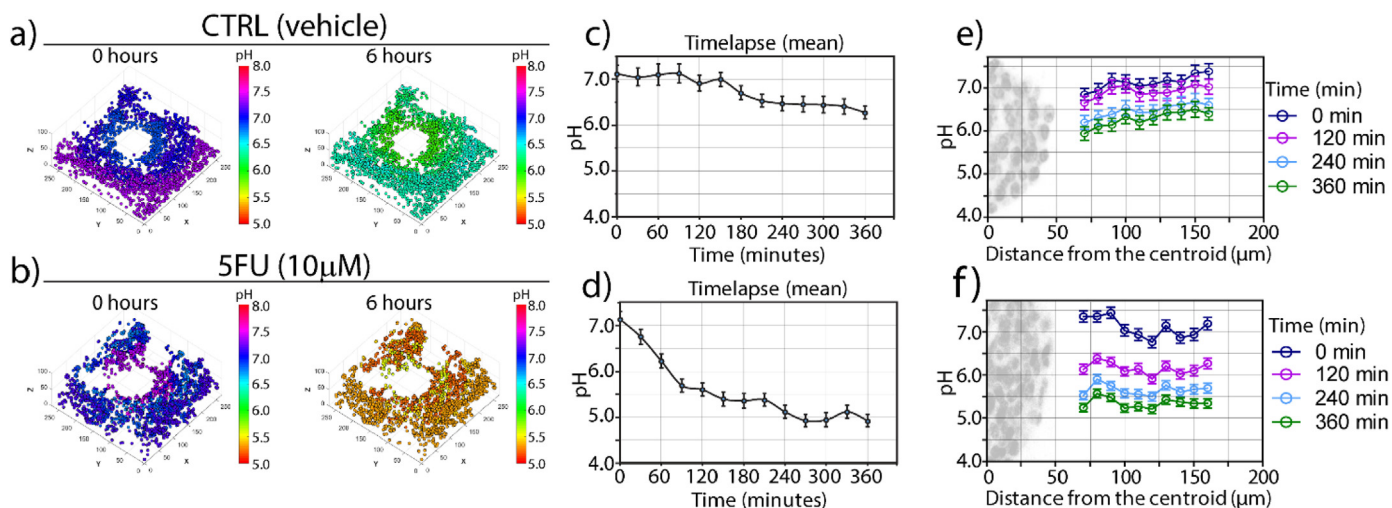

Fig. 9. Spatio-temporal pH representation of HCT116 spheroids in thermosensitive Ch/Pec hydrogels. (a,b) 3D (x, y, z) scatter plots of microparticles-pH sensors at 0 min and 360 min with relative pH colormaps (false colors) of control (vehicle) (a) and treated (5FU, 10 μM for 24 h) (b) spheroids. **(c,d)** Quantification of the pH over time of the experiments in **a** and in **b**, respectively. Data are expressed as means ± SD. **(e,f)** Quantification of the pH at different distances from the centroid of the spheroid is reported for control **(e)** and treated **(f)**, respectively. Data are expressed as means (error bars are omitted for clarity).

Importantly, when the pH response within Ch/Pec hydrogels was evaluated at different distances from the spheroid's centroids (scheme in Figs. 8a and 9e-f) then the scenario change.

Specifically, in control condition at time 0 the pH showed a gradient distribution with values that were acidic in the close proximity of the cells' spheroids (at 50 μm from the centroid) respect to that one detected by the sensors located in the most distal part of the spheroid's centroid (150 μm from the centroid) (see Fig. 9e and Video S5). The pH detected in the microenvironment decreased over time, but the gradient was

maintained, with a higher concentration of protons which was always detected near the spheroid respect to that one registered at 150 μm from the spheroid's centroid (Fig. 9e). These phenomena can be the result of high glycolytic cancer cell metabolism [25], which is common in CRC [53,60] and observed for the first time, with higher spatio-temporal resolution, by using the pH-sensing Ch/Pec hydrogel system. Indeed, the detection of such metabolic gradient resembles some of the features of tumor microenvironment observed *in vivo* [61,62], thus supporting the use of Ch/Pec hydrogel as *in vitro* 3D cell culture tools for CRC spheroids

models. Interestingly, in 5FU treated spheroid the pH detected in the microenvironment was affected and no gradient could be observed (Fig. 9f and Video S6).

Supplementary video related to this article can be found at https://doi.org/10.1016/j.mtbio.2023.100655.

These data support with promote the use of pH-sensing Ch/Pec + hydrogels as a suitable CRC platform for drug screening and personalized medicine. Therefore, starting from patient-derived explants of colorectal cancer, short term culture can be integrated in such a system and the response to drug treatment can be evaluated within 24 h using as a readout the pH metabolic variation detected, in space and time, by the pH-sensing Ch/Pec hydrogel.

3. Conclusion

CRC spheroids and pH sensors were encapsulated within thermoresponsive chitosan-pectin (Ch/Pec) hydrogel yielding to a hybrid platform for the simultaneous support of spheroids culture and the spatiotemporal extracellular pH mapping. Stability, rheological and morphological properties of Ch/Pec hydrogels embedding pH sensors (Ch/Pec +) were compared to those of Ch/Pec hydrogels without pH sensors (Ch/Pec –) showing that, overall, the presence of pH sensors did not affect the features of the hybrid hydrogel.

Proton gradients generated by CRC spheroids in the presence or absence of drug treatment were detected through 4D (x,y,z,t) confocal imaging of embedded ratiometric pH sensors. Results showed that in the treated spheroids the acidification of the microenvironment was faster and more pronounced over time. Even more interesting, when pH response within Ch/Pec hydrogels was evaluated at different distances from the spheroid's centroids, the pH showed a gradient distribution in the control condition with more acidic values in close proximity of the spheroids, resembling the cell metabolic features observed *in vivo* in the tumor microenvironment, while in the treated spheroids no gradients were observed. These data support the use of pH-sensing hybrid Ch/Pec hydrogels for the standardization of *in vitro* 3D tumor models for drug-response and personalized medicine [63]. Such pH-sensing hybrid hydrogels can be successfully paired with automated computational analyses to rapidly monitor the metabolism of patient-derived spheroids during drug testing in a matter of hours *vs.* days or weeks in patients. Additional sensors (*e.g.*, for oxygen detection) could be integrated into the hydrogels and their application for noninvasive and accurate *in situ* microenvironment investigation of pH and oxygen could be exploited thanks to the *in vivo* thermosensitivity and injectability of Ch/Pec hydrogels.

4. Experimental section/methods

Preparation of hybrid pH-sensing thermoresponsive hydrogel in chitosan and pectin. Low molecular weight chitosan (cat n° 448,869, Sigma Aldrich) (Ch), pectin from citrus peel (galacturonic acid ≥74.0% dried basis) (cat n° P9135, Sigma Aldrich) (Pec) and beta-glycerophosphate (βGP) (cat n° 50,020, Sigma Aldrich) were used for hydrogel preparation, as previously described [17,18]. Optical ratiometric pH sensors based on SiO_2 microparticles functionalized with FITC, as pH indicator probe, and RBITC, as reference dye, were synthetized as previously described [54,64]. The synthesized pH sensors showed a particle diameter of 1.548 ± 0.009 μm (Fig. S3a) and a regular spherical shape (Figs. S3b–d). Importantly, because of the known dynamic swelling in water, average hydrodynamic sizes resulted being slightly bigger than the ones evaluated under dry condition [65]. The hybrid pH-sensing thermoresponsive Ch/Pec hydrogel was obtained by solubilizing separately Ch powder (w/v) in aqueous solution of hydrochloric acid (HCl) 0.1 M and Pec powder (w/v) in ultrapure water (Milli-Q) under stirring at room temperature (RT) overnight. The Ch solution was further centrifuged at 1500 rpm for 5′ at 4 °C to remove bubbles. The two solutions were mixed in an optimized volume ratio (50:50) and centrifuged at

1500 rpm for 5' at 4 °C. Then, a gelling agent solution, *i.e.*, 0.04 M βGP as final concentration, was added to the Ch/Pec formulation and mixed with complete DMEM in a 3:1.5 ratio (Fig. 1a) before adding 40 μL of pH sensors [5.38×10^6 particles/mL stock solution] per each mL of Ch/Pec formulation followed by gentle mixing for 2 min. The Ch/Pec formulation containing sensors was subsequently centrifuged at 1500 rpm for 20 s to remove bubbles. Next, 30 μL Ch/Pec hydrogel containing SiO_2 microparticle-based optical pH sensors were plated into an 8-well chamber slides (cat n° 80,827, Ibidi GmbH, Graefelfing, Germany) and placed at physiological temperature (37 °C) to induce a sol-gel transition. This protocol led to obtain a homogeneous, injectable, thermoresponsive and completely bubble-free hydrogel able to sense the pH in the cellular microenvironment. Ch/Pec hydrogel formulations without sensors were used as control. The two hydrogel formulations, with and without pH sensors (hereinafter referred to as "Ch/Pec +" and "Ch/Pec –"), were characterized in terms of physico-chemical properties, such as swelling measurements, weight stability in cell culture conditions, porosity evaluation and mechanical properties, through both rheological analyses and compression tests.

Swelling Test. The swelling ability of the hydrogels was assessed by evaluating the weight variations of the hydrogel samples up to 12 days. Briefly, after thermal gelation (2 h at 37 °C), the samples were frozen at −20 °C overnight and then lyophilized overnight (LIO 5 P freeze dryer, Cinquepascal). The weight of each sample was measured in the dry state and immediately after hydration in phosphate-buffered saline (PBS) at 37 °C, then monitored at different time points (1′, 2′, 3′, 4′, 5′, 10′, 20′, 30', 1 h, 2 h, 6 h, 24 h, 48 h, 72 h, 12 d). The swelling ratio (SR) percentage was calculated according to the following Formula (1), where W_{dry} is the initial dry weight of the hydrogel and W_{wet} is the weight of the hydrogel after hydration in PBS and incubation at 37 °C:

$$SR\ (\%) = \left[\left(W_{wet} - W_{dry} \right)\ /\ W_{dry} \right] x\ 100 \qquad (1)$$

In vitro stability. The non-enzymatic degradation of the hydrogel was evaluated up to 30 days through gravimetric measurements. After 2 h of incubation at 37 °C, Ch/Pec + and Ch/Pec – hydrogel samples were weighed (t = 0) and the weight was then monitored at different incubation times at 37 °C in PBS. The percentage of weight loss (WL) was calculated according to the following Formula (2), where W_0 is the initial weight of the hydrogel at t = 0 after thermal gelation at 37 °C and W_i is the weight of the hydrogel after its hydration in PBS at 37 °C at the different time points (0, 1 h, 2 h, 24 h, 48 h, 72 h, 96 h, 7 d, 14 d, 21 d, 30 d):

$$WL\ (\%) = \left[(W_0 - W_i)\ /\ W_0 \right] x\ 100 \qquad (2)$$

Rheological analysis. An exhaustive rheological analysis was performed on Ch/Pec + and Ch/Pec – hydrogels using a rheometer (Physica MCR 301, Anton Paar) equipped with a two plates geometry (plate diameter 25 mm, gap distance 0.5 mm) and connected to a circulating water bath. The following rheological tests were performed on fully formed hydrogels: i) strain sweep from 0.1 to 100% strain at a constant frequency of 1.0 Hz, to check for the linear viscoelastic (LVE) limit, ii) frequency sweep from 0.01 to 100 Hz at the LVE strain amplitude determined in the strain sweep, to find an appropriate value of frequency for the time sweep, iii) time sweep at the verified strain and frequency values, *i.e.* 10% strain and 1 Hz of frequency, to obtain the hydrogel storage modulus (G′) and loss modulus (G″), iv) temperature sweep at constant shear strain (10%), constant frequency (1 Hz), while the temperature was increased from 5 to 50 °C at a rate of 1 °C/min, to obtain the hydrogel storage modulus (G′) and loss modulus (G″) as function of temperature. Each test was performed in duplicate.

Compression test. To evaluate the influence of pH sensors addition on hydrogel's stiffness, uniaxial compression tests have been performed on both Ch/Pec + and Ch/Pec – hydrogel formulations in wet conditions at RT. Fully formed hydrogel samples (diameter = 12 mm) were loaded between two impermeable and non-lubricated compression plates and

compressed at a displacement velocity of 2 mm/min, using a universal uniaxial machine (ZwickiLine 1 kN, Zwick Roell). The Young's modulus (E) was then calculated as the slope of the linear part of the stress-strain curves at low strain values (0–10%) for both hydrogel formulations. The respective mean values were compared, and the data statistically analyzed (n = 4).

Morphological analysis and porosity measurement. The morphology of the samples was analyzed by scanning electron microscopy (SEM), using a Sigma 300 VP FE-SEM (Carl Zeiss AG) in secondary electron (SE) mode. Before SEM analyses, the fully formed hydrogel samples were dehydrated in a graded ethanol-water series to 100% ethanol (20, 50, 70, 90, 100%), 5 min for each concentration, and critical point dried (K850 CPD, Quorum Technologies). A cross section of about 1.5 mm was cut in half with a razor, mounted on aluminum stubs and sputter-coated with 10 nm gold (CCU-010 LV, Safematic) to prevent charge accumulation. Once SEM images were acquired, an imaging software (ImageJ bundled with 64-bit Java 1.8.0_172) was used to measure the pore diameter of hydrogel formulations with and without pH sensors. Briefly, two SEM images at magnification 10 × were analyzed for each formulation, measuring the diameter as an average of two diameter measurements for each pore, for approximately a total of 115 pores per type.

Cell culture. Colorectal carcinoma cells (HCT 116, ATCC CCL-247, LGC Standards) were cultured in DMEM with 4.5 g L^{-1} glucose and sodium pyruvate without L-glutamine (cat n° 17-205-CV, Corning) supplemented with 2 mM L-glutamine (cat n°25,030,024, Gibco), 10% Fetal Bovine Serum (FBS) (cat n° 35-079-CV, Corning), 100 U mL $^{-1}$ penicillin and 100 μg mL^{-1} streptomycin (cat n° 15,140,122, Gibco). Cells were incubated at 37 °C with 95% of humidity and 5% of carbon dioxide (CO_2) and 0.05% Trypsin-Ethylenediaminetetraacetic acid (Trypsin-EDTA 1X) (cat n° 59430C, Sigma Aldrich) was used regularly to split cells every 2–3 days until 90% confluence was reached.

HCT116 Spheroids formation and encapsulation in Ch/Pec hydrogels. Approximately 250.000 HCT116 cells were seeded in ULA T75 flasks for around five days to allow spheroids formation. Before encapsulation, HCT116 spheroids were labelled using a Hoechst 33,342 Fluorescent Stain for nuclei (cat n° 14,533, Sigma Aldrich), in order to assess their distribution and growth within the hydrogels. Importantly, HCT116 spheroids with diameter below 200 μm were separated with pluriStrainer (200 μm mesh sizes), before mixing them with the Ch/Pec hydrogel formulations containing pH sensors (see Fig. 1a). The hydrogel loaded with both spheroids and pH sensors was spotted in each 4-well chamber slide (cat n° 80,427, IBIDI GmbH, Graefelfing, Germany), about 30 μL/spot, and incubated at 37 °C for 20 min to allow sample gelation. Afterwards, each well was covered with 250 μL of DMEM that was replaced after 10 min. The samples were incubated for 2 h at 37 °C and HCT 116 spheroids were observed under fluorescence microscope (EVOS m7000, Thermo Fisher Scientific) and CLSM (LSM700, Carl Zeiss AG).

Biocompatibility assay of Ch-Pec hydrogel formulations. HCT116 cells were seeded in ULA T75 flasks to allow spheroids formation and encapsulated after 3 days in Ch/Pec + containing unlabeled SiO_2 microparticles or Ch/Pec – hydrogels. Cell viability was evaluated until day 7 through Live/Dead assay. Briefly, Ch/Pec + or Ch/Pec-hydrogels were incubated in complete medium containing Calcein AM (Sigma-Aldrich, Darmstadt, Germany) and propidium iodide (PI, Sigma-Aldrich, Darmstadt, Germany), to a final concentration of 0.25 μM and 10 μM respectively. After 45 min of incubation, the hydrogels were washed with PBS 1X and incubated for 30 min with Hoechst 33,342 (Sigma Aldrich, Darmstadt, Germany) to stain cell nuclei. Then, spheroids without hydrogels were plated into an 8-well chamber slides (IBIDI, Berlin, Germany) previously functionalized with 0.1 mg mL^{-1} of poly-lysine (Sigma Aldrich, Darmstadt, Germany) in order to facilitate the adhesion on the well and were used as control. Representative images were captured at days 1, 3, and 7 of culture using a CLSM (LSM700, Carl Zeiss AG) at 20× magnification. The maximum projections of z-stack images were obtained using Image J software. In parallel, Ch/Pec + or Ch/Pec – hydrogels viability was evaluated through PrestoBlue cell viability

Reagent (Thermo Fisher scientific) at days 1, 3 and 7. At each time point, the culture medium in which spheroids grew for each condition was moved into a Corning® 96 well-plates and 5 μL of PrestoBlue Reagent were added into each well and incubated for 1 h at 37 °C and 5% CO_2. The fluorescent signal was obtained using a microplate reader (ClarioStarPlus, BMG Labtech, DE), at 535 nm of excitation wavelength and 590 nm of emission wavelength. Spheroids without hydrogels were used as a control and the values of medium without cells and containing Ch/Pec + or Ch/Pec – hydrogels were subtracted from those of the samples.

Live cell imaging. HCT116 spheroids encapsulated in Ch/Pec + hydrogels were placed onto 4-well chamber slides, as described before. Then, samples were gently washed three times in complete medium for 10 min and incubated with pH 7.0 adjusted cell medium, while Ch/Pec + hydrogels intended for the setup of the ratiometric calibration curve were incubated with pH adjusted cell media (from pH 4.0 to pH 8.0). Next, samples were left to equilibrate for 30 min before being mounted on a CLSM (objective Plan-Apochromat 20 × /0.8) and imaged under controlled temperature (37 °C) and CO_2 (4%). For live cell imaging, z-stack images were acquired at regular interval of 30 min (λ_{exc}: 488 nm, λ_{em}: 510–594 nm; λ_{exc}: 405 nm, λ_{em}: 415–735 nm; λ_{exc}: 555 nm; λ_{em}: LP560 nm; 319.77 × 319.77 pixels; average line, 2). CLSM images were processed using ImageJ software and analyzed by a customized algorithm developed with GNU Octave (see also experimental section).

Computational method for image processing and analysis. 4D (x,y,z,t) CLSM images were automatically analyzed with a custom algorithm written in GNU Octave (version 6.2.0), modified starting from [54]. Briefly, the algorithm took as input the two fluorescence signals of the pH sensors (FITC and RBITC). The RBITC channel was pre-processed z-by-z, converted to grayscale, binarized and segmented by a watershed transformation [66]. For each time point t, images were stored in three-dimensional matrices. Then, objects (*i.e.*, pH sensors) in 3D were defined by direct connectivity of the binary RBITC images along the z-axis, resulting in a 3D binary matrix, which was used as a mask to extract positions and mean fluorescence intensity ratios of the particles belonging to the original FITC and RBITC signals images: for each pH sensor particle, the pixel-by-pixel ratio between FITC and RBITC fluorescence intensities (I_{FITC}/I_{RBITC}) was calculated. To obtain I_{FITC}/I_{RBITC} measured from a specific sensor, results were averaged along the pixels composing that sensor. pH values were extracted by passing I_{FITC}/I_{RBITC} data in a pH- I_{FITC}/I_{RBITC} calibration curve (Fig. 7), which was previously obtained by incubating Ch/Pec hydrogels with sensors in pH-adjusted cell media. Finally, pH was also monitored globally over time, by calculating, for each time point, the mean and the standard deviation of the pH measured by the single sensors.

Contemporarily, the fluorescence channel belonging to the cell nuclei (Hoechst) was pre-processed, converted to grayscale and binarized in order to extract the centroid, C_s (x,y,z), and the ray, R_s, of the whole spheroid. Then, the Euclidean distance between C_s and the sensors was calculated, to select sensors found within spherical shells iteratively 10 μm further from the spheroid's ray R_s (Fig. 8a). In the end, the mean and the standard deviation of the pH measured by the single sensors belonging to each spherical shell were extracted.

Statistical analysis. All experiments were performed in quadruplicate (unless differently stated) and the results are reported as the mean ± standard deviation. Data analysis and graphing were performed with Microsoft Excel 2019, GraphPad Prism software (v. 7.0.4–2018) and Origin 2022 (SR1). Statistical differences were considered significant at p < 0.05. Concerning the compression tests, GraphPad Prism software (v. 8.4.2) was employed to perform statistical analysis, using two-way ANOVA analysis.

Author contributions

Funding and study supervision: LLDM, FG, GG, AP, RR; Study design: LLDM, FG, AP, RR, VO; Data acquisition and data analyses: FG, HI, GM, RR, VO, FS, SF; Writing—original draft preparation: LLDM, FG, GM, RR,

VO; writing, review and editing: LLDM, FG, AP, RR, VO, SF. All authors have read and agreed to the published version of the manuscript.

Declaration of competing interest

The authors declare that they have no known competing financial interests or personal relationships that could have appeared to influence the work reported in this paper.

Data availability

Data will be made available on request.

Appendix A. Supplementary data

Supplementary data to this article can be found online at https://doi.org/10.1016/j.mtbio.2023.100655.

References

[1] F. Bray, J. Ferlay, I. Soerjomataram, R.L. Siegel, L.A. Torre, A. Jemal, Global cancer statistics 2018: GLOBOCAN estimates of incidence and mortality worldwide for 36 cancers in 185 countries, Ca - Cancer J. Clin. 68 (2018) 394–424, https://doi.org/10.3322/CAAC.21492.
[2] R.L. Siegel, K.D. Miller, A. Jemal, Cancer statistics, Ca - Cancer J. Clin. 69 (2019) 7–34, https://doi.org/10.3322/caac.21551, 2019.
[3] J.P. Griffin-Sobel, Gastrointestinal cancers: screening and early detection, Semin. Oncol. Nurs. 33 (2017) 165–171, https://doi.org/10.1016/j.soncn.2017.02.004.
[4] F. Castro, C. Leite Pereira, M. Helena Macedo, A. Almeida, M. José Silveira, S. Dias, A. Patrícia Cardoso, M. José Oliveira, B. Sarmento, Advances on colorectal cancer 3D models: the needed translational technology for nanomedicine screening, Adv. Drug Deliv. Rev. 175 (2021) 113824, https://doi.org/10.1016/j.addr.2021.06.001.
[5] J. Thiele, Y. Ma, S.M.C. Bruekers, S. Ma, W.T.S. Huck, 25th anniversary article: designer hydrogels for cell cultures: a materials selection guide, Adv. Mater. 26 (2014) 125–148, https://doi.org/10.1002/adma.201302958.
[6] A. Kamb, What's wrong with our cancer models? Nat. Rev. Drug Discov. 4 (2005) 161–165, https://doi.org/10.1038/NRD1635.
[7] M. Kapałczyńska, T. Kolenda, W. Przybyła, M. Zajączkowska, A. Teresiak, V. Filas, M. Ibbs, R. Bliźniak, Ł. Łuczewski, K. Lamperska, 2D and 3D cell cultures – a comparison of different types of cancer cell cultures, Arch. Med. Sci. 14 (2018) 910, https://doi.org/10.5114/AOMS.2016.63743.
[8] P.S. Thakuri, C. Liu, G.D. Luker, H. Tavana, Biomaterials-based approaches to tumor spheroid and organoid modeling, Adv Healthc Mater 7 (2018), 1700980, https://doi.org/10.1002/adhm.201700980.
[9] E. Reidy, N.A. Leonard, O. Treacy, A.E. Ryan, A 3D view of colorectal cancer models in predicting therapeutic responses and resistance, Cancers 13 (2021) 1–22, https://doi.org/10.3390/CANCERS13020227.
[10] M. Cavo, D. Delle Cave, E. D'Amone, G. Gigli, E. Lonardo, L.L. del Mercato, A synergic approach to enhance long-term culture and manipulation of MiaPaCa-2 pancreatic cancer spheroids, Sci. Rep. 10 (2020) 1, https://doi.org/10.1038/s41598-020-66908-8, 10 (2020) 1–11.
[11] M.W. Laschke, M.D. Menger, Life is 3D: boosting spheroid function for tissue engineering, Trends Biotechnol. 35 (2017) 133–144, https://doi.org/10.1016/J.TIBTECH.2016.08.004.
[12] D. Blondel, M.P. Lutolf, Bioinspired hydrogels for 3D organoid culture, Chimia 73 (2019) 81–85, https://doi.org/10.2533/CHIMIA.2019.81.
[13] E.A. Aisenbrey, W.L. Murphy, Synthetic alternatives to Matrigel, Nat. Rev. Mater. 5 (2020) 539, https://doi.org/10.1038/S41578-020-0199-8.
[14] J. Thiele, Y. Ma, S.M.C. Bruekers, S. Ma, W.T.S. Huck, 25th anniversary article: designer hydrogels for cell cultures: a materials selection guide, Adv. Mater. 26 (2014) 125–148, https://doi.org/10.1002/adma.201302958.
[15] A.P. Dhand, J.H. Galarraga, J.A. Burdick, Enhancing biopolymer hydrogel functionality through interpenetrating networks, Trends Biotechnol. 39 (2021) 519–538, https://doi.org/10.1016/J.TIBTECH.2020.08.007.
[16] H. Liu, Y. Wang, K. Cui, Y. Guo, X. Zhang, J. Qin, Advances in hydrogels in organoids and organs-on-a-chip, Adv. Mater. 31 (2019), 1902042, https://doi.org/10.1002/ADMA.201902042.
[17] G. Morello, A. Polini, F. Scalera, R. Rizzo, G. Gigli, F. Gervaso, Preparation and characterization of salt-mediated injectable thermosensitive chitosan/pectin hydrogels for cell embedding and culturing, Polymers 13 (2021) 2674, https://doi.org/10.3390/polym13162674.
[18] G. Morello, A. Quarta, A. Gaballo, L. Moroni, G. Gigli, A. Polini, F. Gervaso, A thermo-sensitive chitosan/pectin hydrogel for long-term tumor spheroid culture, Carbohydr. Polym. 274 (2021), 118633, https://doi.org/10.1016/j.carbpol.2021.118633.
[19] G. Morello, G. de Iaco, G. Gigli, A. Polini, F. Gervaso, Chitosan and pectin hydrogels for tissue engineering and in vitro modeling, Gels 9 (2023) 132, https://doi.org/10.3390/gels9020132.
[20] I. Zarandona, C. Bengoechea, E. Álvarez-Castillo, K. de la Caba, A. Guerrero, P. Guerrero, 3D printed chitosan-pectin hydrogels: from rheological characterization to scaffold development and assessment, Gels 7 (2021) 175, https://doi.org/10.3390/gels7040175.
[21] P. Matricardi, C. di Meo, T. Coviello, W.E. Hennink, F. Alhaique, Interpenetrating Polymer Networks polysaccharide hydrogels for drug delivery and tissue engineering, Adv. Drug Deliv. Rev. 65 (2013) 1172–1187, https://doi.org/10.1016/j.addr.2013.04.002.
[22] X. Jing, F. Yang, C. Shao, K. Wei, M. Xie, H. Shen, Y. Shu, Role of hypoxia in cancer therapy by regulating the tumor microenvironment, Mol. Cancer 18 (2019) 157, https://doi.org/10.1186/s12943-019-1089-9.
[23] S. Prasad, A. Chandra, M. Cavo, E. Parasido, S. Fricke, Y. Lee, E. D'Amone, G. Gigli, C. Albanese, O. Rodriguez, L.L. del Mercato, Optical and magnetic resonance imaging approaches for investigating the tumour microenvironment: state-of-the-art review and future trends, Nanotechnology 32 (2020), 062001, https://doi.org/10.1088/1361-6528/ABC208.
[24] N.U. Dharmaratne, A.R. Kaplan, P.M. Glazer, Targeting the hypoxic and acidic tumor microenvironment with pH-sensitive peptides, Cells 10 (2021) 1–14, https://doi.org/10.3390/CELLS10030541.
[25] C. Corbet, O. Feron, Tumour acidosis: from the passenger to the driver's seat, Nat. Rev. Cancer 17 (2017) 577–593, https://doi.org/10.1038/NRC.2017.77.
[26] N. Piasentin, E. Milotti, R. Chignola, The control of acidity in tumor cells: a biophysical model, Sci. Rep. 10 (2020) 1–10, https://doi.org/10.1038/s41598-020-70396-1, 2020) 1–14.
[27] E. Boedtkjer, L. Bunch, S.F. Pedersen, Physiology, pharmacology and pathophysiology of the pH regulatory transport proteins NHE1 and NBCn1: similarities, differences, and implications for cancer therapy, Curr. Pharmaceut. Des. 18 (2012) 1345–1371, https://doi.org/10.2174/138161212799504830.
[28] P. Swietach, R.D. Vaughan-Jones, A.L. Harris, A. Hulikova, The chemistry, physiology and pathology of pH in cancer, Phil. Trans. Biol. Sci. 369 (2014), 20130099, https://doi.org/10.1098/rstb.2013.0099.
[29] F. Serio, A.F. da Cruz, A. Chandra, C. Nobile, G.R. Rossi, E. D'Amone, G. Gigli, L.L. del Mercato, C.C. de Oliveira, Electrospun polyvinyl-alcohol/gum Arabic nanofibers: biomimetic platform for in vitro cell growth and cancer nanomedicine delivery, Int. J. Biol. Macromol. 188 (2021) 764–773, https://doi.org/10.1016/J.IJBIOMAC.2021.08.069.
[30] F. Serio, N. Silvestri, S. Kumar Avugadda, G.E.P. Nucci, S. Nitti, V. Onesto, F. Catalano, E. D'Amone, G. Gigli, L.L. del Mercato, T. Pellegrino, Co-loading of doxorubicin and iron oxide nanocubes in polycaprolactone fibers for combining Magneto-Thermal and chemotherapeutic effects on cancer cells, J. Colloid Interface Sci. 607 (2022) 34–44, https://doi.org/10.1016/J.JCIS.2021.08.153.
[31] D.D. Cave, R. Rizzo, B. Sainz, G. Gigli, L.L. del Mercato, E. Lonardo, The revolutionary roads to study cell-cell interactions in 3D in vitro pancreatic cancer models, Cancers 13 (2021) 1–19, https://doi.org/10.3390/CANCERS13040930.
[32] M. Turetta, F. del Ben, G. Brisotto, E. Biscontin, M. Bulfoni, D. Cesselli, A. Colombatti, G. Scoles, G. Gigli, L.L. del Mercato, Emerging Technologies for cancer research: towards personalized medicine with microfluidic platforms and 3D tumor models, Curr. Med. Chem. 25 (2018) 4616, https://doi.org/10.2174/0929867325666180605122633.
[33] M. Cavo, F. Serio, N.R. Kale, E. D'Amone, G. Gigli, L.L. del Mercato, Electrospun nanofibers in cancer research: from engineering of in vitro 3D cancer models to therapy, Biomater. Sci. 8 (2020) 4887–4905, https://doi.org/10.1039/D0BM00390E.
[34] J.D. Piper, C. Li, C.-J. Lo, R. Berry, Y. Korchev, L. Ying, D. Klenerman, Characterization and application of controllable local chemical changes produced by reagent delivery from a nanopipet, J. Am. Chem. Soc. 130 (2008) 10386–10393, https://doi.org/10.1021/ja8022253.
[35] S.K. Parks, J. Chiche, J. Pouyssegur, pH control mechanisms of tumor survival and growth, J. Cell. Physiol. 226 (2011) 299–308, https://doi.org/10.1002/JCP.22400.
[36] X. Gu, Y. Ma, Y. Liu, Q. Wan, Measurement of mitochondrial respiration in adherent cells by Seahorse XF96 cell mito stress test, STAR Protoc 2 (2021), 100245, https://doi.org/10.1016/J.XPRO.2020.100245.
[37] Y. Zhang, Y. Takahashi, S.P. Hong, F. Liu, J. Bednarska, P.S. Goff, P. Novak, A. Shevchuk, S. Gopal, I. Barozzi, L. Magnani, H. Sakai, Y. Suguru, T. Fujii, A. Erofeev, P. Gorelkin, A. Majouga, D.J. Weiss, C. Edwards, A.P. Ivanov, D. Klenerman, E.v. Sviderskaya, J.B. Edel, Y. Korchev, High-resolution label-free 3D

mapping of extracellular pH of single living cells, Nat. Commun. 10 (2019) 5610, https://doi.org/10.1038/S41467-019-13535-1.

[38] A. Anemone, L. Consolino, F. Arena, M. Capozza, D.L. Longo, Imaging tumor acidosis: a survey of the available techniques for mapping in vivo tumor pH, Cancer Metastasis Rev. 38 (2019) 25–49, https://doi.org/10.1007/S10555-019-09782-9.

[39] A. Jaworska, K. Malek, A. Kudelski, Intracellular pH – advantages and pitfalls of surface-enhanced Raman scattering and fluorescence microscopy – a review, Spectrochim. Acta Mol. Biomol. Spectrosc. 251 (2021), 119410, https://doi.org/10.1016/j.saa.2020.119410.

[40] A.I. Pérez-Jiménez, D. Lyu, Z. Lu, G. Liu, B. Ren, Surface-enhanced Raman spectroscopy: benefits, trade-offs and future developments, Chem. Sci. 11 (2020) 4563–4577, https://doi.org/10.1039/D0SC00809E.

[41] M. Xu, X. Ma, T. Wei, Z.-X. Lu, B. Ren, In situ imaging of live-cell extracellular pH during cell apoptosis with surface-enhanced Raman spectroscopy, Anal. Chem. 90 (2018) 13922–13928, https://doi.org/10.1021/acs.analchem.8b03193.

[42] G. Yang, Q. Zhang, Y. Liang, H. Liu, L.L. Qu, H. Li, Fluorescence-SERS dual-signal probes for pH sensing in live cells, Colloids Surf. A Physicochem. Eng. Asp. 562 (2019) 289–295, https://doi.org/10.1016/J.COLSURFA.2018.11.036.

[43] M. Xu, X. Ma, T. Wei, Z.-X. Lu, B. Ren, In situ imaging of live-cell extracellular pH during cell apoptosis with surface-enhanced Raman spectroscopy, Anal. Chem. 90 (2018) 13922–13928, https://doi.org/10.1021/acs.analchem.8b03193.

[44] A. Chandra, S. Prasad, G. Gigli, L.L. del Mercato, Fluorescent nanoparticles for sensing, Frontiers of Nanoscience 16 (2020) 117–149, https://doi.org/10.1016/B978-0-08-102828-5.00006-1.

[45] L.L. del Mercato, L.G. Passione, D. Izzo, R. Rinaldi, A. Sannino, F. Gervaso, Design and characterization of microcapsules-integrated collagen matrixes as multifunctional three-dimensional scaffolds for soft tissue engineering, J. Mech. Behav. Biomed. Mater. 62 (2016) 209–221, https://doi.org/10.1016/J.JMBBM.2016.05.009.

[46] I.L. Moldero, A. Chandra, M. Cavo, C. Mota, D. Kapsokalyvas, G. Gigli, L. Moroni, L.L. del Mercato, I.L. Moldero, C. Mota, L. Moroni, A. Chandra, M. Cavo, G. Gigli, D. Kapsokalyvas, Probing the pH microenvironment of mesenchymal stromal cell cultures on additive-manufactured scaffolds, Small 16 (2020), 2002258, https://doi.org/10.1002/SMLL.202002258.

[47] A. Chandra, S. Prasad, H. Iuele, F. Colella, R. Rizzo, E. D'Amone, G. Gigli, L.L. del Mercato, Highly sensitive fluorescent pH microsensors based on the ratiometric dye pyranine immobilized on silica microparticles, Chemistry 27 (2021) 13318–13324, https://doi.org/10.1002/CHEM.202101568.

[48] L.L. del Mercato, M. Moffa, R. Rinaldi, D. Pisignano, Ratiometric organic fibers for localized and reversible ion sensing with micrometer-scale spatial resolution, Small 11 (2015) 6417–6424, https://doi.org/10.1002/SMLL.201502171.

[49] M. de Luca, M.M. Ferraro, R. Hartmann, P. Rivera-Gil, A. Klingl, M. Nazarenus, A. Ramirez, W.J. Parak, C. Bucci, R. Rinaldi, L.L. del Mercato, Advances in use of capsule-based fluorescent sensors for measuring acidification of endocytic compartments in cells with altered expression of V-ATPase subunit V 1 G 1, ACS Appl. Mater. Interfaces 7 (2015) 15052–15060, https://doi.org/10.1021/acsami.5b04375.

[50] W. Niu, L. Fan, M. Nan, Z. Li, D. Lu, M.S. Wong, S. Shuang, C. Dong, Ratiometric emission fluorescent pH probe for imaging of living cells in extreme acidity, Anal. Chem. 87 (2015) 2788–2793, https://doi.org/10.1021/ac504109h.

[51] V. Onesto, S. Forciniti, F. Alemanno, K. Narayanankutty, A. Chandra, S. Prasad, A. Azzariti, G. Gigli, A. Barra, A. De Martino, D. De Martino, L.L. del Mercato, Probing single-cell fermentation fluxes and exchange networks via pH-sensing

hybrid nanofibers, ACS Nano 17 (2023) 3313–3323, https://doi.org/10.1021/acsnano.2c06114.

[52] R. Sjöback, J. Nygren, M. Kubista, Absorption and fluorescence properties of fluorescein, Spectrochim. Acta Mol. Biomol. Spectrosc. 51 (1995), https://doi.org/10.1016/0584-8539(95)01421-. L7–L21.

[53] E. Boedtkjer, S.F. Pedersen, The acidic tumor microenvironment as a driver of cancer, Annu. Rev. Physiol. 82 (2020) 103–126, https://doi.org/10.1146/ANNUREV-PHYSIOL-021119-034627.

[54] R. Rizzo, V. Onesto, S. Forciniti, A. Chandra, S. Prasad, H. Iuele, F. Colella, G. Gigli, L.L. del Mercato, A pH-sensor scaffold for mapping spatiotemporal gradients in three-dimensional in vitro tumour models, Biosens. Bioelectron. 212 (2022), 114401, https://doi.org/10.1016/J.BIOS.2022.114401.

[55] G.S. Offeddu, L. Mohee, R.E. Cameron, Scale and structure dependent solute diffusivity within microporous tissue engineering scaffolds, J. Mater. Sci. Mater. Med. 31 (2020) 1–11, https://doi.org/10.1007/S10856-020-06381-x.

[56] L. Neufeld, H. Bianco-Peled, Pectin–chitosan physical hydrogels as potential drug delivery vehicles, Int. J. Biol. Macromol. 101 (2017) 852–861, https://doi.org/10.1016/J.IJBIOMAC.2017.03.167.

[57] X. Du, J. Zhai, X. Li, Y. Zhang, N. Li, X. Xie, Hydrogel-based optical ion sensors: principles and challenges for point-of-care testing and environmental monitoring, ACS Sens. 6 (2021) 1990–2001, https://doi.org/10.1021/acssensors.1c00756.

[58] F. le Guern, V. Mussard, A. Gaucher, M. Rottman, D. Prim, Fluorescein derivatives as fluorescent probes for pH monitoring along recent biological applications, Int. J. Mol. Sci. 21 (2020) 1–23, https://doi.org/10.3390/IJMS21239217.

[59] D. Neri, C.T. Supuran, Interfering with pH regulation in tumours as a therapeutic strategy, Nat. Rev. Drug Discov. 10 (2011) 767–777, https://doi.org/10.1038/nrd3554, 10. 10 (2011).

[60] Y. Kato, S. Ozawa, C. Miyamoto, Y. Maehata, A. Suzuki, T. Maeda, Y. Baba, Acidic extracellular microenvironment and cancer, Cancer Cell Int. 13 (2013) 89, https://doi.org/10.1186/1475-2867-13-89.

[61] M. Anderson, A. Moshnikova, D.M. Engelman, Y.K. Reshetnyak, O.A. Andreev, Probe for the measurement of cell surface pH in vivo and ex vivo, Proc. Natl. Acad. Sci. USA 113 (2016) 8177–8181, https://doi.org/10.1073/pnas.1608247113.

[62] P. Altea-Manzano, A.M. Cuadros, L.A. Broadfield, S. Fendt, Nutrient metabolism and cancer in the in vivo context: a metabolic game of give and take, EMBO Rep. 21 (2020), https://doi.org/10.15252/embr.202050635.

[63] S. Ding, C. Hsu, Z. Wang, N.R. Natesh, R. Millen, M. Negrete, N. Giroux, G.O. Rivera, A. Dohlman, S. Bose, T. Rotstein, K. Spiller, A. Yeung, Z. Sun, C. Jiang, R. Xi, B. Wilkin, P.M. Randon, I. Williamson, D.A. Nelson, D. Delubac, S. Oh, G. Rupprecht, J. Isaacs, J. Jia, C. Chen, J.P. Shen, S. Kopetz, S. McCall, A. Smith, N. Gjorevski, A.-C. Walz, S. Antonia, E. Marrer-Berger, H. Clevers, D. Hsu, X. Shen, Patient-derived micro-organospheres enable clinical precision oncology, Cell Stem Cell 29 (2022) 905–917.e6, https://doi.org/10.1016/j.stem.2022.04.006.

[64] A. Chandra, S. Prasad, F. Alemanno, M. de Luca, R. Rizzo, R. Romano, G. Gigli, C. Bucci, A. Barra, L.L. del Mercato, Fully automated computational approach for precisely measuring organelle acidification with optical pH sensors, ACS Appl. Mater. Interfaces 14 (2022) 18133–18149, https://doi.org/10.1021/acsami.2c00389.

[65] M. Kersting, M. Olejnik, N. Rosenkranz, K. Loza, M. Breisch, A. Rostek, G. Westphal, J. Bünger, N. Ziegler, A. Ludwig, M. Köller, C. Sengstock, M. Epple, Subtoxic cell responses to silica particles with different size and shape, Sci. Rep. 10 (2020), 21591, https://doi.org/10.1038/s41598-020-78550-5.

[66] F. Meyer, Topographic distance and watershed lines, Signal Process. 38 (1994) 113–125, https://doi.org/10.1016/0165-1684(94)90060-4.